Journal of Advanced Marine Engineering and Technology, Vol. 49, No. 4, pp. 295~306, 2025
J. Advanced Marine Engineering and Technology (JAMET)
https://doi.org/10.5916/jamet.2025.49.4.295

ISSN 2234-7925 (Print)
ISSN 2765-4796 (Online)
Original Paper

Effect on mooring line separation angles including one-line failure for 15 MW floating offshore wind turbine system

Se Hwan Park[1] · Yong Hun Jung[2] · Woo Chul Chung[†]

(Received July 1, 2025 ; Revised July 24, 2025 ; Accepted August 14, 2025)

Abstract: This study investigated the dynamic behavior of a 15 MW floating offshore wind turbine system under mooring line failure conditions with varying mooring line separation angles (10°, 20°, and 30°). A numerical model was developed using commercial software OrcaFlex, and both time- and frequency-domain simulations were performed under extreme environmental conditions. The analysis focused on the failure of Mooring Line 2 in a six-line catenary configuration. The time-domain results revealed that the mooring line layout had a minimal effect under intact conditions; however, after the one-line failure, the 30° case exhibited the largest increases in surge, sway, roll, and yaw motions owing to the greater asymmetry in the restoring forces. In addition, the mooring line tensions were redistributed, with significant increases in Mooring Lines 1, 3, and 4. The bending moment of the power cable at the touchdown point peaked in the 30° configuration. The frequency-domain analysis showed dominant ultralow-frequency responses, particularly in the 10° case. These findings highlight the critical role of the mooring layout in the structural response and provide insights into the design of mooring systems and potential mitigation strategies for failure scenarios.

Keywords: Floating offshore wind turbine, Mooring line angle, Dynamic response analysis, Power cable, Bending moment, Mooring line failure

1. Introduction

Amid growing concerns about global warming and climate change, countries worldwide are intensifying their efforts to achieve net-zero carbon emissions. Consequently, interest in renewable energy has increased significantly, and governments and industries are actively promoting policies to reduce fossil fuel consumption and expand the use of ecofriendly energy sources, as noted by Jo **[1]**.

Furthermore, Kim *et al.* **[2]** recognized wind energy, along with solar, hydropower, and geothermal energy as key renewable sources. Owing to its high efficiency and environment-friendly nature, wind energy has been the focus of extensive global research and investment. Wind power does not emit greenhouse gases during operation and is considered cost-effective in the long term. Consequently, renewable energy is one of the fastest-growing sectors and is expected to become a major source of global electricity supply by 2050, as reported by the International Renewable Energy Agency **[3]**.

In addition, wind energy in the ocean can be considered a key contributor to the future energy mix as one of the major renewable energy sources; however, installation areas are limited owing to geographical constraints. Onshore wind power is limited in that noise and environmental problems occur during large-scale installation, and fixed offshore wind power cannot be installed in the deep sea above a depth of approximately 50 m. Park *et al.* **[4]** explored the initial structural design of jacket-type substructures for 12 MW fixed-bottom offshore wind turbines, highlighting design challenges for large-capacity systems. Accordingly, floating offshore wind power technology, which can operate even in the deep sea, is attracting attention as a solution for the next generation of wind energy, and studies to solve this problem are actively underway.

Min *et al.* **[5]** analyzed the economic feasibility of domestic offshore wind farm development, highlighting the need for

† Corresponding Author (ORCID: http://orcid.org/ 0000-0003-1125-5423): Assistant Professor, Division of Mechanical Engineering, National Korea Marine & Ocean University, 727, Taejong-ro, Yeongdo-gu, Busan 49112, Korea, E-mail: wcchung@kmou.ac.kr, Tel: +82-51-410-4361

1 M. S. Candidate, Division of Mechanical Engineering, National Korea Marine & Ocean University, E-mail: tpghks0905@g.kmou.ac.kr, Tel: +82-51-410-4974

2 Research Engineer, Offshore Power System Research Team, R&D Center, Taihan Cable & Solution Co., Ltd., E-mail: yhjung@taihan.com, Tel: +82-2-316-9104

alternative deployment methods.

Unlike conventional fixed offshore wind power, floating offshore wind power does not require the installation of a complex and difficult foundation on the seabed and can be used in deep waters regardless of the seabed terrain. In addition, as it can be installed far from the coast, stronger and more constant winds can be utilized, thereby increasing power generation and minimizing conflict with fishing or marine environments. In particular, the development of a floating offshore wind platform that can use large turbines of 15 MW or more is in progress, which is expected to further improve economic feasibility and power generation efficiency, as noted by KRISO **[6]**.

Accordingly, studies are continuously being conducted to optimize the design and secure the stability of floating offshore wind power systems, and various related technical approaches are being developed. Lee *et al.* **[7]** analyzed how wind–wave direction mismatch and yaw error affect the output performance and structural stability of a 15 MW floating offshore wind turbine (FOWT). Ahn *et al.* **[8]** compared the response characteristics among the operating conditions of a 15 MW-class FOWT with a semi-submersible platform.

Chen *et al.* **[9]** conducted systematic comparisons among various simulation tools, such as OpenFAST and Charm3D, to evaluate their accuracy in representing the FOWT dynamics. Jin *et al.* **[10]** also assessed the dynamic behavior of semi-submersible FOWTs using Morison-equation-based approaches. One of the key technical challenges related to floating offshore wind power generators is securing the dynamic stability of structures. Floating platforms are continuously exposed to various environmental loads, such as wind, waves, and currents, which directly affect the performance of the generator and the kinetic characteristics of the floating body. To control this external force, floating wind power generators are generally fixed to the bottom of the sea through a mooring system; however, when abnormal conditions, such as damage or fracture of a mooring line or extreme marine environments, occur, the behavior of the structure becomes unstable, which may degrade the stability of the entire power generation system.

Accordingly, it is also important to analyze the transient response characteristics that occur when a mooring line is damaged in a floating wave-sea wind power complex power generation structure, as studied by Bae and Lee **[11]**.

This study aimed to quantitatively evaluate the effect of mooring line arrangement angles on the dynamic response of a 15 MW FOWT when a mooring line failure occurs. In addition, the variations in tension acting on the mooring lines and power cables under marine environmental loads, as well as the distribution of bending moments in the touchdown zone where the power cable contacts the seabed, were analyzed to assess the influence of the mooring layout design on the overall system stability.

2. Target Structure

2.1 System Description

In this study, OrcaFlex was used to analyze the dynamic response of the entire system, including an FOWT and a power cable. OrcaFlex is a commercial simulation software widely used in the analysis of offshore structures and mooring systems, and is suitable for evaluating the kinetic performance of floating structures and the stability of mooring systems. The FOWT model used in this study was based on the K03 15 MW semi-submersible example model provided by Orcina **[12]**, and a mooring system consisting of six mooring lines was applied.

The mass properties of the floating platform, including the moment of inertia and center of mass (CoM), were defined based on the model configuration. In particular, the CoM was located at approximately x = 2.80 m, y = 0.04 m, z = 92.61 m, slightly offset in the forward (x+) and upward (z+) directions relative to the platform origin. This configuration reflects the mass distribution effect of the overhanging rotor–nacelle assembly and was used as the input for both the static and dynamic simulations. A summary of the CoM coordinates is presented in **Table 1**.

To ensure the reliability of the analysis, a six-degree-induced static analysis was first performed without an external force in the environment. The results are summarized in **Table 2**. Subsequently, dynamic analysis was performed to reflect the actual motion characteristics of the entire system. At this stage, the wind turbine was set to a parked condition, indicating that the rotor blades were not rotating, and no power generation was considered. This allowed us to focus solely on structural responses to environmental loads.

Figure 1 shows the overall structure of an offshore wind power system. This model was designed to enhance the station-keeping capability of floating bodies owing to marine environmental loads, such as wind, waves, and current loads, through a mooring system consisting of six mooring lines. The mooring line number is shown in **Figure 2(a)**, and the connection and arrangement positions of the mooring lines are visually expressed. In addition, the arrangement angle between the mooring lines is

confirmed, as shown in **Figure 2**. The specifications of the mooring line are summarized in **Table 3**, and in this study, a stud-link chain with a bar diameter of 0.33 m was applied as a mooring line. The mooring line controlled the movement of the floating body and maintained its stability. The power cable was designed with a diameter of 0.2 m and was configured to stably transmit electricity to the seabed. This value is consistent with previous studies on dynamic power cables used in floating offshore wind systems, as reported by Rentschler *et al*. **[13]**.

The global coordinate positions of the mooring lines and power cables, including both the hang-off (fairlead) and anchor points, are summarized in **Table 4**. The horizontal radii from the platform center to each anchor point were 837.707, 837.062, and 836.011 m for the 10°, 20°, and 30° mooring line separation angles, respectively, as presented in **Table 5**. At the fairlead connection, each mooring line was modeled with a pinned (hinged) boundary condition that allowed free rotation while restricting translational motion. This setup represents the typical catenary mooring behavior and enables a realistic simulation of the dynamic response of the platform.

Table 1: CoM position of the floating platform

Centre of Mass (m)		
X	Y	Z
2.796	0.0388	92.613

Table 2: Static analysis of six degrees of freedom without environmental loads

Platform	Degree of freedom	Value
Hull	Surge(m)	-1.045
	Sway(m)	-0.004
	Heave(m)	-0.322
	Roll(deg)	-0.018
	Pitch(deg)	1.295
	Yaw(deg)	-0.00

Table 3: Specifications of mooring lines

Mooring properties	Mooring line	Power cable
Material	Studlink R4	Umbilical
Unstretched length(m)	850	670
Bar Diameter(m)	0.33	0.2
Mass per unit length(te/m)	0.695	0.072
Axial stiffness (kN)	3.27E+06	2.88E+05
Min breaking loads (kN)	52.52e3kN	-

Table 4: Coordinate points according to the global coordinate system

Variable	Coordinate point	
(ML = Mooring Line)	(x, y, z)	
	Hang-off or End A	Anchor or End B
FPSO center	(0, 0, 0)	
Power cable	(0.0.-20)	(-600, 0, -192)
10deg ML 1	(58, 0 -14)	(834.5, -73, -192)
10deg ML 2	(58, 0 -14)	(834.5, 73, -192)
10deg ML 3	(-29, 50.23, -14)	(-354, 759.2, -192)
10deg ML 4	(-29, 50.23, -14)	(-480.5, 686.21, -192)
10deg ML 5	(-29, -50.23, -14)	(-480.5, -686.21, -192)
10deg ML 6	(-29, -50.23, -14)	(-354, -759.2, -192)
20deg ML 1	(58, 0 -14)	(825, -145.5, -192)
20deg ML 2	(58, 0 -14)	(825, 145.5, -192)
20deg ML 3	(-29, 50.23, -14)	(-291, 784.9, -192)
20deg ML 4	(-29, 50.23, -14)	(-534.2, 644.4, -192)
20deg ML 5	(-29, -50.23, -14)	(-534.2, -644.4, -192)
20deg ML 6	(-29, -50.23, -14)	(-291, -784.9, -192)
30deg ML 1	(58, 0 -14)	(810, -206.7, -192)
30deg ML 2	(58, 0 -14)	(810, 206.7, -192)
30deg ML 3	(-29, 50.23, -14)	(-226, 804.9, -192)
30deg ML 4	(-29, 50.23, -14)	(-584.1, 598.1, -192)
30deg ML 5	(-29, -50.23, -14)	(-584.1, -598.1, -192)
30deg ML 6	(-29, -50.23, -14)	(-226, -804.9, -192)

Table 5: Horizontal radius

Horizontal radius (m)		
10deg	20deg	30deg
837.707	837.062	836.011

Table 6: Natural frequencies

Platform	Deg	Degree of freedom	Frequency (rad/s)
Hull	10	Surge	0.11
		Sway	0.071
		Heave	0.462
		Roll	0.331
		Pitch	0.263
		Yaw	0.142
	20	Surge	0.109
		Sway	0.074
		Heave	0.465
		Roll	0.332
		Pitch	0.267
		Yaw	0.143
	30	Surge	0.108
		Sway	0.075
		Heave	0.465
		Roll	0.332
		Pitch	0.266
		Yaw	0.146

In addition, the natural frequency of the substructure, which is a key parameter for reviewing whether the system resonates and secures dynamic stability in advance, is listed in **Table 6**. As the

natural frequency directly affects the kinetic response of the entire system, the system was constructed by sufficiently considering the natural frequency when designing the simulation model.

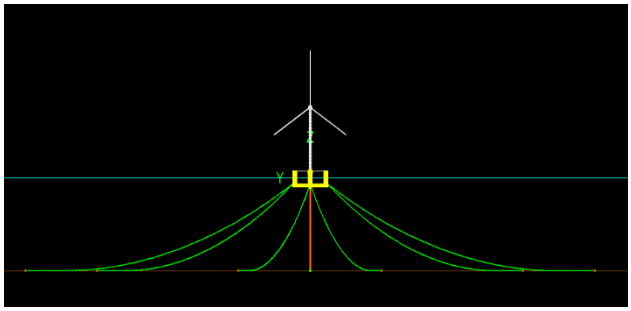

(a) Front view

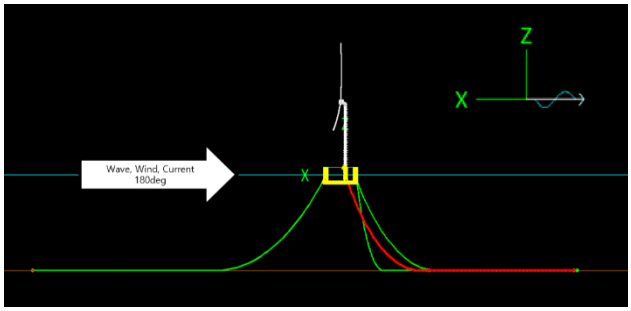

(b) Left view

Figure 1: Overall structure of the offshore wind system

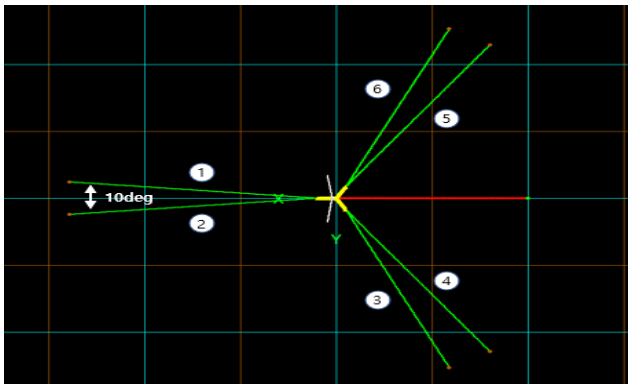

(a) Mooring line separation angle of 10°

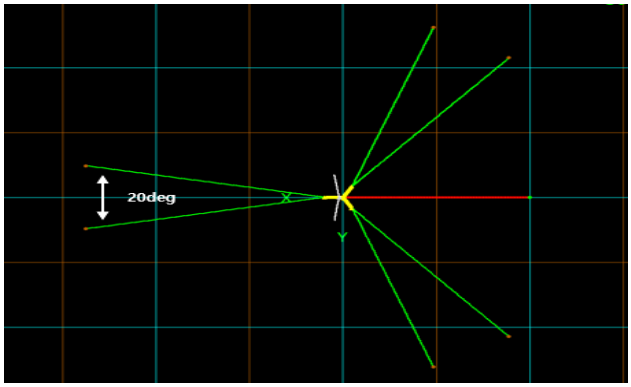

(b) Mooring line separation angle of 20°

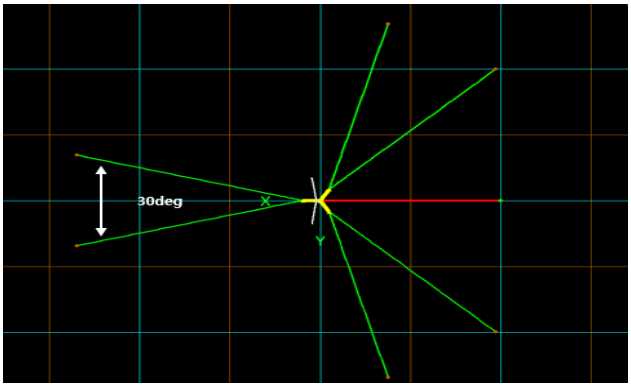

(c) Mooring line separation angle of 30°

Figure 2: Top view

Table 7: Environmental conditions

	Variable	Unit	Value
Wave	Spectrum	[-]	JONSWAP
	Peak enhancement factor	[-]	2.5
	Hs	[m]	11.9
	Tp	[s]	14.2
Current	Depth	[m]	192
	Velocity	[m/s]	2.0
Wind	Spectrum	[-]	API
	Speed	[m/s]	40

2.2 Environmental Conditions

The environmental conditions used in this study are listed in **Table 7**. The environmental conditions were set to extreme conditions as described by Lee *et al.* **[14]**. The target offshore area was assumed to be on the east side of North America in an extreme environment, and the depth was assumed to be 192 m.

These conditions represent a 50-year return period, which is commonly used in offshore structural designs to ensure conservative safety margins. The selected wave height and wind speed values are consistent with the regional design standards for floating offshore wind applications in deep waters.

The peak enhancement factor was set to 2.5, the significant wave height was set to 11.9 m, and the peak period was set to 14.2 s. For the ocean current condition, the flow rate on the water surface was assumed to be 2.0 m/s, and the wind speed was set to an average of 40 m/s by applying the API spectrum. All the environmental loads were considered to act in the same direction of 180° (collinear).

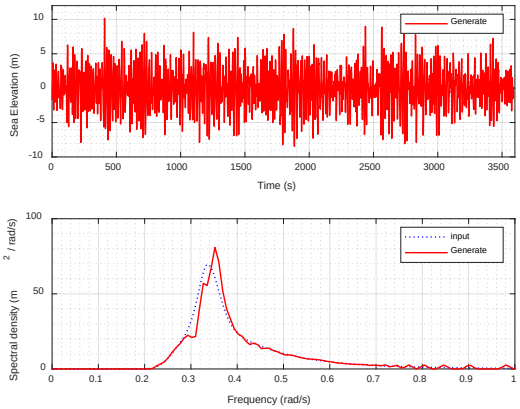

Figure 3: Wave time history (up), input vs. generated spectrum comparison (down)

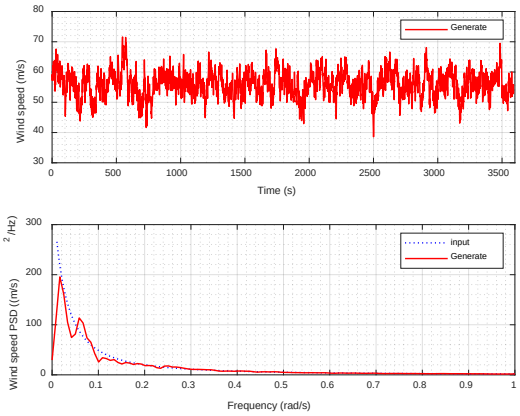

Figure 4: Wind time history (up), input vs. generated spectrum comparison (down)

Figures 3 and **4** show the time history graphs of the wave and wind used in the analysis and the frequency response, respectively. A comparison between the input and generated spectra after the analysis in each figure showed that the two frequency responses were highly consistent. These results indicated that the environmental conditions set in this study were accurately reflected in the analysis and supported the reliability and accuracy of the results.

3. Results and Discussion

3.1 Time Domain

In this study, three mooring line separation angles (10°, 20°, and 30°) were considered to evaluate the dynamic response of a floating structure in the event of mooring line failure. The analysis was based on the six degrees of freedom (DOF) of the floater (surge, sway, heave, roll, pitch, and yaw). Additionally, changes in the tension and bending moments were assessed for all the mooring lines and power cables.

3.1.1 Floater Displacements

Figures 5 and **6** present the dynamic responses when all the mooring lines are intact. Across all the six DOFs, no significant differences were observed in the mooring line separation angle. This indicated that, under intact conditions, the mooring line separation angle had a limited influence on the overall motion of the floater. In the mooring failure simulations, the mooring line ML_#2 was intentionally broken at 1800 s. This timing was consistent across all cases and was critical for interpreting the response variations presented in the following sections. These results are presented to clarify that the dynamic changes observed after mooring line failure are primarily caused by the failure itself rather than by the difference in the mooring line arrangement angles. In other words, the dynamic response under intact conditions is provided as a base, enabling a quantitative comparison of the relative impact of motion amplification and instability in subsequent mooring failure scenarios.

Figure 7 shows the translational motion responses under the failure of mooring line #2 (ML_#2). Both the surge and sway amplitudes increased in all the separation angle cases after failure, with the 30° case showing the most significant increase. This is attributed to the alignment of the environmental load direction with the location of ML_#2. Thus, its failure caused a sharp reduction in the restoring force in that direction, directly amplifying the surge response. In the 10° case, owing to the narrower separation angle between the mooring lines, load redistribution occurred more efficiently, resulting in a smaller increase in the translational motion.

In contrast, the heave responses showed minimal variation compared with the surge and sway, as the vertical motion was less sensitive to the loss of the horizontal restoring force.

Figure 8 shows the rotational response. Notably, the roll and yaw motions shifted most significantly in the 30° configuration. The wider separation between the remaining mooring lines following the ML_#2 failure resulted in a larger asymmetric restoring moment, intensifying the rotational motion. In particular, the yaw was directly influenced by the asymmetry caused by failure, leading to greater instability at 30°.

However, the pitch responses remained nearly identical across all cases, suggesting that the wave loads in the longitudinal direction had a dominant influence and that the mooring line failure had a minimal effect in this DOF.

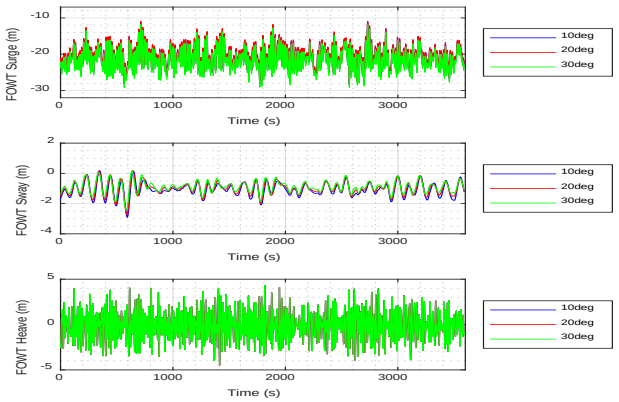

Figure 5: Time-domain surge, sway, and heave responses of the FOWT under the intact mooring condition

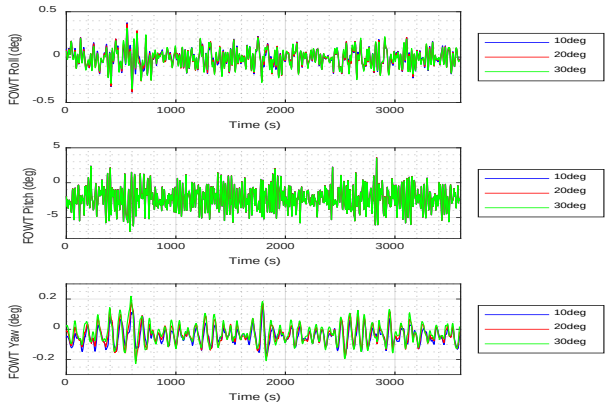

Figure 6: Time-domain roll, pitch, and yaw responses of the FOWT under the intact mooring condition

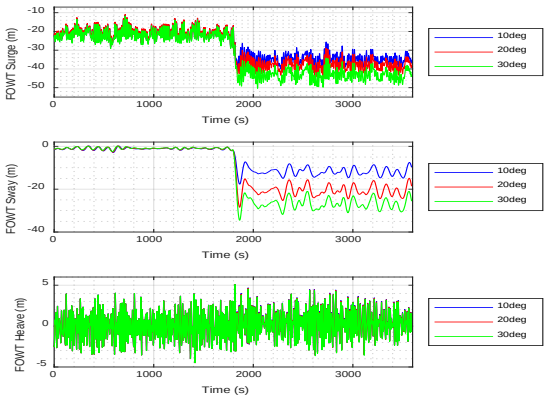

Figure 7: Time-domain surge, sway, and heave responses of the FOWT under the failure of Mooring Line #2

For a quantitative comparison and analysis of the results shown in **Figures 5–8**, the corresponding data are organized in **Tables 8–11**.

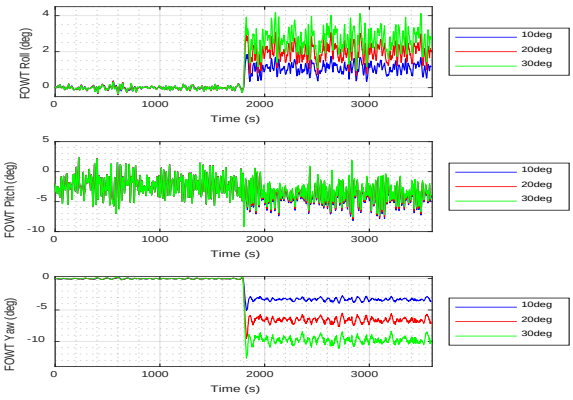

Figure 8: Time-domain roll, pitch, and yaw responses of the FOWT under the failure of Mooring Line #2

Table 8: Time-domain surge, sway, and heave responses of the FOWT under the intact mooring condition

Motion	Deg	Period (s)	Min.	Max.	Mean	Std.
Surge [m]	10	0~ 3600 (s)	-28.37	-11.22	-20.89	2.74
	20		-28.08	-10.89	-20.58	2.75
	30		-29.18	-11.77	-21.6	2.77
Sway [m]	10		-2.91	0.18	-1.07	0.45
	20		-2.74	0.18	-0.99	0.42
	30		-2.43	0.15	-0.9	0.38
Heave [m]	10		-4.48	4.33	-0.08	1.52
	20		-4.49	4.32	-0.09	1.52
	30		-4.48	4.32	-0.09	1.52

Table 9: Time-domain roll, pitch, and yaw responses of the FOWT under the intact mooring condition

Motion	Deg	Period (s)	Min.	Max.	Mean	Std.
Roll [deg]	10	0~ 3600 (s)	-0.39	0.38	-0.01	0.09
	20		-0.38	0.37	-0.01	0.09
	30		-0.35	0.32	-0.01	0.09
Pitch [deg]	10		-6.99	3.62	-2.24	1.51
	20		-6.98	3.61	-2.24	1.51
	30		-6.98	3.54	-2.26	1.50
Yaw [deg]	10		-0.17	0.15	-0.05	0.05
	20		-0.21	0.18	-0.04	0.06
	30		-0.23	0.22	-0.03	0.07

Table 10: Time-domain surge, sway, and heave responses of the FOWT under the failure of Mooring Line #2

Motion	Deg	Period (s)	Min.	Max.	Mean	Std.
Surge [m]	10	1800~ 3600 (s)	-41.6	-17.07	-34.69	2.93
	20		-44.87	-16.79	-37.69	3.17
	30		-50.33	-17.92	-42.76	3.55
Sway [m]	10		-17.65	-1.99	-11.59	2.22
	20		-28.46	-1.79	-20.23	3.37
	30		-34.53	-1.54	-26.31	3.96
Heave [m]	10		-3.51	5.09	0.44	1.50
	20		-3.57	5.09	0.4	1.49
	30		-3.63	5.09	0.35	1.49

Table 11: Time-domain roll, pitch, and yaw responses of the FOWT under the failure of Mooring Line #2

Motion	Deg	Period (s)	Min.	Max.	Mean	Std.
Roll [deg]	10	1800~ 3600 (s)	-0.13	1.84	1.07	0.30
	20		-0.14	3.21	1.94	0.49
	30		-0.15	4.18	2.64	0.64
Pitch [deg]	10		-9.04	1.74	-4.00	1.53
	20		-9.10	1.82	-3.83	1.50
	30		-9.15	1.83	-3.62	1.46
Yaw [deg]	10		-5.08	0.13	-3.31	0.38
	20		-9.54	0.16	-6.57	0.71
	30		-12.67	0.18	-9.71	0.97

3.1.2 Mooring Line and Power Cable

The effective tension was measured at the fairlead connection point of each mooring line where it interfaces with the floating platform.

Figure 9 shows the effective tension of the mooring lines ML_#1–ML_#6. **Figure 10** presents the tension measured at three locations along the power cable: the fairlead, midpoint, and anchor. Figure 11 illustrates the bending moment responses at the touchdown point (TDP) of the power cable, which is the most critical location.

During the one-line failure simulation, the mooring line ML_#2 was intentionally broken at 1800 s, resulting in a complete loss of tension and subsequent load redistribution among the remaining lines. ML_#1, ML_#3, and ML_#4 experienced increased tension, whereas ML_#5 and ML_#6 exhibited a relative decrease. Notably, ML_#3 exhibited the greatest increase in tension in the 30° configuration, which was attributed to the asymmetric rotational motions, particularly yaw and roll, which concentrated the tensile loads in that direction.

Conversely, ML_#5 and ML_#6, which were located on the opposite side of the rotational direction, experienced a relative decrease in tension. In the 10° condition, the narrower spacing between the mooring lines helped suppress structural twisting, allowing the redistributed loads to be more evenly shared among the lines.

Figure 10 shows a comparison of the tensions at the fairlead, midpoint, and anchor of the power cables. Following the mooring line failure, the fairlead experienced the largest fluctuation in tension as the motion of the floating platform was directly transferred to the upper end of the cable. This effect was most pronounced for the 30° condition. While similar trends were observed at the midpoint and anchor, the magnitude of the variation was smaller. Notably, even though the anchor point was fixed to

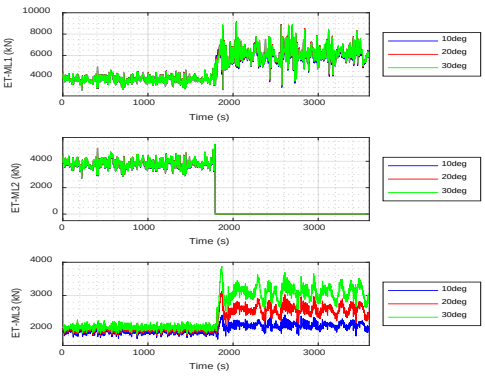

(a) Mooring lines #1, #2, #3

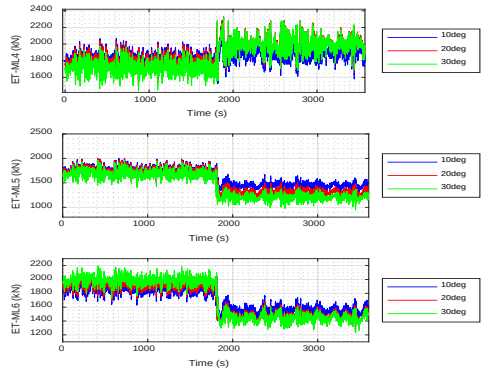

(b) Mooring lines #4, #5, #6

Figure 9: Time-domain effective tension of the mooring lines under the failure of Mooring Line #2

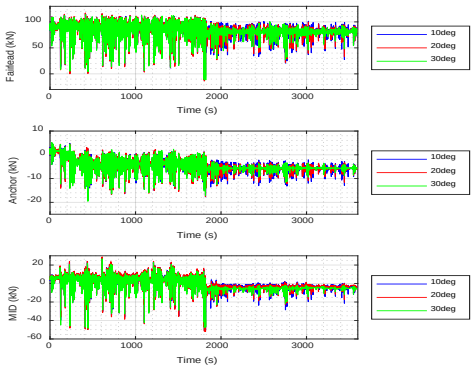

Figure 10: Time-domain effective tension of the power cable under the failure of Mooring Line #2

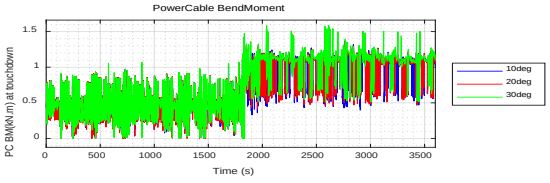

Figure 11: Time-domain bending moment of the power cable under the failure of Mooring Line #2, TDP

Table 12: Time-domain effective tension of the mooring lines under the failure of Mooring Line #2

Line	Deg	Period (s)	Min.	Max.	Mean	Std.
ML_1 (kN)	10deg	0~1800(s)	2700	5200	3757	310
		1800~3600(s)	2776	9041	6041	770
	20 deg	0~1800(s)	2722	5194	3765	306
		1800~3600(s)	2796	9173	6133	780
	30 deg	0~1800(s)	2705	5161	3751	301
		1800~3600(s)	2830	9141	6131	775
ML_2 (kN)	10deg	0~1800(s)	2702	5267	3781	317
		1800~3600(s)	0	3748	0.21	27
	20 deg	0~1800(s)	2723	5305	3811	320
		1800~3600(s)	0	3803	0.21	28
	30 deg	0~1800(s)	2711	5283	3807	318
		1800~3600(s)	0	3819	0.21	28
ML_3 (kN)	10deg	0~1800(s)	1704	2170	1932	69
		1800~3600(s)	1684	2417	2106	97
	20 deg	0~1800(s)	1777	2218	1990	67
		1800~3600(s)	1862	3131	2568	168
	30 deg	0~1800(s)	1831	2271	2044	65
		1800~3600(s)	1945	3874	3085	249
ML_4 (kN)	10deg	0~1800(s)	1553	2067	1811	73
		1800~3600(s)	1524	2187	1884	83
	20 deg	0~1800(s)	1502	2041	1772	75
		1800~3600(s)	1562	2327	1993	100
	30 deg	0~1800(s)	1435	1973	1717	75
		1800~3600(s)	1550	2324	1986	99
ML_5 (kN)	10deg	0~1800(s)	1504	2003	1764	74
		1800~3600(s)	1242	1896	1448	64
	20 deg	0~1800(s)	1450	1999	1733	76
		1800~3600(s)	1055	1838	1306	67
	30 deg	0~1800(s)	1406	1966	1687	76
		1800~3600(s)	947	1783	1211	67
ML_6 (kN)	10deg	0~1800(s)	1628	2087	1873	69
		1800~3600(s)	1311	2036	1554	68
	20 deg	0~1800(s)	1688	2147	1931	68
		1800~3600(s)	1256	2042	1472	76
	30 deg	0~1800(s)	1729	2196	1985	66
		1800~3600(s)	1226	2097	1453	81

the seabed, the structural motion was transmitted indirectly, resulting in tension variation at that location.

Figure 11 shows the time-domain bending moment response at the TDP of the power cable. After the failure of ML_#2 at 1800 s, the increased motion of the floater resulted in a significant increase in the bending moment at the seabed contact point. The largest bending response was observed at 30°, which can be attributed to the maximized asymmetry in the restoring forces caused by the wider mooring line spacing. This asymmetry led to greater surge, roll, and yaw motions, and these combined motions induced stronger and more repetitive bending and tension–release cycles at the lower end of the cable. To evaluate the structural safety of the remaining mooring lines after failure, the maximum

Table 13: Time-domain effective tension of the power cable under the failure of Mooring Line #2

Line	Deg	Period (s)	Min.	Max.	Mean	Std.
Fairlead (kN)	10	0~1800(s)	1.9	116	89.8	9.0
		1800~3600(s)	-11.9	107	82.4	6.4
	20	0~1800(s)	0.07	117	90.1	9.1
		1800~3600(s)	-13.7	107	82.1	6.1
	30	0~1800(s)	4.4	114	89.3	8.8
		1800~3600(s)	-11.7	105	81.2	5.7
Anchor (kN)	10	0~1800(s)	-19	4.9	-3.0	2.0
		1800~3600(s)	-17.6	1.3	-5.7	0.7
	20	0~1800(s)	-18.8	5.0	-3.0	2.0
		1800~3600(s)	-17.5	1.2	-5.8	0.6
	30	0~1800(s)	-19.5	5.2	-3.1	2.0
		1800~3600(s)	-17.2	0.9	-5.7	0.5
MID (kN)	10	0~1800(s)	-48.6	27.7	5.9	5.2
		1800~3600(s)	-50.6	15.4	-3.3	2.4
	20	0~1800(s)	-49.9	28.8	6.2	5.3
		1800~3600(s)	-52	16.5	-3.5	2.3
	30	0~1800(s)	-48.4	26.8	5.0	4.9
		1800~3600(s)	-47.8	13.2	-5.2	1.9

Table 14: Time-domain bending moment of the power cable under the failure of Mooring Line #2, TDP

Line	Deg	Period (s)	Min.	Max.	Mean	Std.
Power cable BM (kN.m) at touch down	10	0~1800(s)	1.36E-03	1.06	0.46	0.16
		1800~3600(s)	1.38E-03	1.41	0.93	0.22
	20	0~1800(s)	1.00E-03	1.05	0.46	0.16
		1800~3600(s)	1.76E-03	1.50	0.98	0.21
	30	0~1800(s)	1.26E-03	1.07	0.48	0.16
		1800~3600(s)	6.17E-04	1.59	1.07	0.18

tension observed in ML_#1 was compared with the minimum breaking load (MBL). Under the 20° separation angle condition, where the highest increase in tension occurred, ML_#1 reached a maximum effective tension of approximately 9,173 kN. Given that the MBL of the Studlink R4 chain is 52,520 kN (as summarized in **Table 2**), this corresponds to approximately 17.5% utilization, indicating that the mooring

system maintained a sufficient safety margin even under extreme failure conditions.

3.2 Spectral Analysis of Time-Domain Responses

In this study, a frequency spectrum analysis was conducted by applying fast Fourier transform (FFT)-based spectral processing to the time-domain simulation results. The time histories of the mooring line tensions, platform motions, and power cable responses were exported from OrcaFlex and post-processed in MATLAB to obtain the corresponding power spectral densities (PSDs).

The PSD was computed separately for the pre-failure (0–1800 s) and post-failure (1800–3600 s) periods using time-domain simulation data. This approach allowed a clearer identification of the inherent frequency characteristics of the system by isolating the dynamic responses before and after failure.

3.2.1 Floater Displacements

Figures 12 and **13** present the frequency spectrum analysis results of the six DOFs—surge, sway, heave, roll, pitch, and yaw—of the FOWT before and after the failure of mooring line ML_#2. Prior to failure (0–1800 s), distinct peaks corresponding to the natural frequencies of the floater were observed across multiple DOFs. In the surge response, a secondary peak appeared at approximately 0.35 rad/s, which is attributed to wave load components. The heave response exhibited two prominent peaks: one at approximately 0.3 rad/s corresponding to the dominant wave excitation frequency, and the other at approximately 0.4 rad/s corresponding to the natural frequency of the heave mode, indicating the coexistence of wave-induced and resonant responses. The pitch response exhibited a distinct natural frequency peak at approximately 0.24 rad/s, whereas the roll and yaw responses displayed relatively small peaks in the low-frequency range.

After the failure (1800–3600 s), a significant increase in energy was observed in the low-frequency range (below approximately 0.05 rad/s), particularly in the surge, sway, roll, and yaw responses, with apparent variations depending on the mooring line angle (10°, 20°, and 30°). This behavior is attributed to the asymmetric restoring forces caused by the mooring line failure, which amplifies the nonlinear low-frequency motions of the floater. In contrast, the heave and pitch responses retained their dominant natural frequency peaks at approximately 0.3–0.4 rad/s and 0.24 rad/s, respectively, indicating that their primary resonant characteristics were largely unaffected by the failure. Overall, the failure of ML_#2 significantly amplified the low-frequency responses in the horizontal and rotational DOFs while

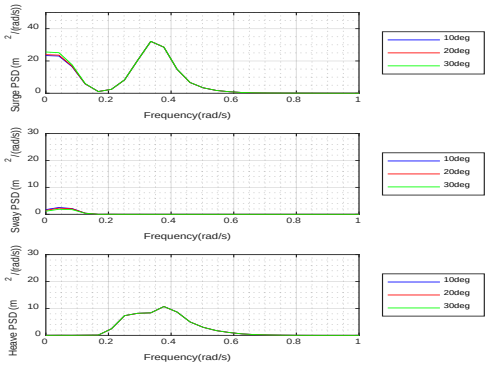

(a) Pre-failure

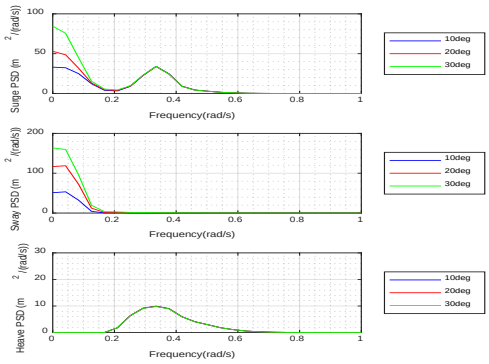

(b) Post-failure

Figure 12: Frequency-domain surge, sway, and heave responses of the FOWT under the failure of Mooring Line #2

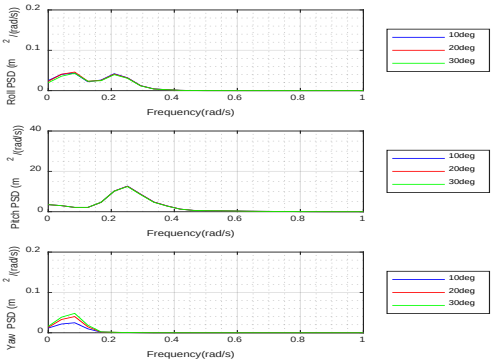

(a) Pre-failure

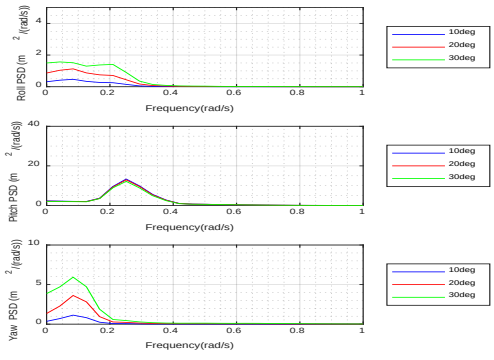

(b) Post-failure

Figure 13: Frequency-domain roll, pitch, and yaw responses of the FOWT under the failure of Mooring Line #2

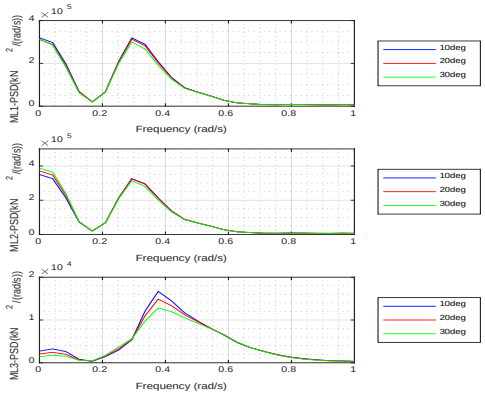

(a) Pre-failure Mooring lines #1, #2, and #3

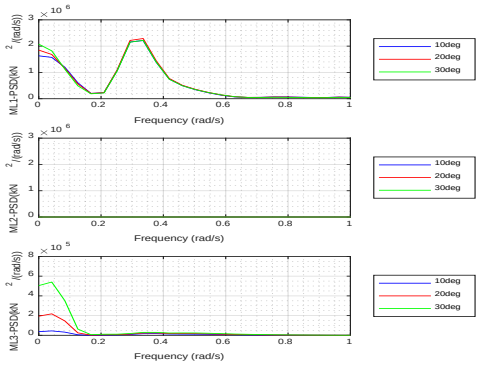

(b) Post-failure Mooring lines #1, #2, and #3

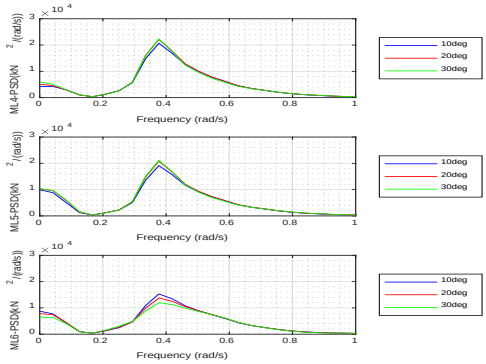

(c) Pre-failure Mooring lines #4, #5, and #6

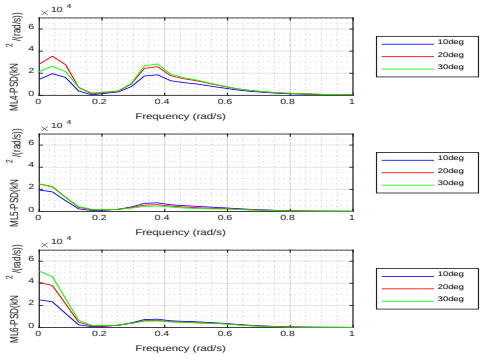

(d) Post-failure Mooring lines #4, #5, #6

Figure 14: Frequency-domain effective tension of the mooring lines under the failure of Mooring Line #2

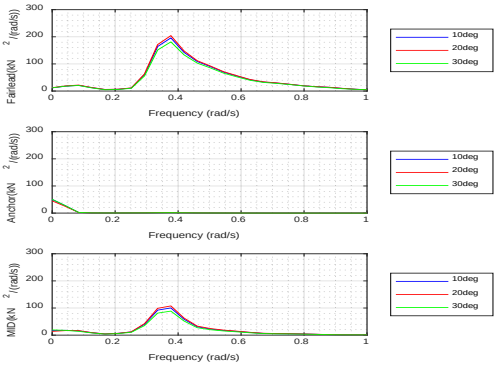

(a) Pre-failure fairlead, anchor, MID on power cable

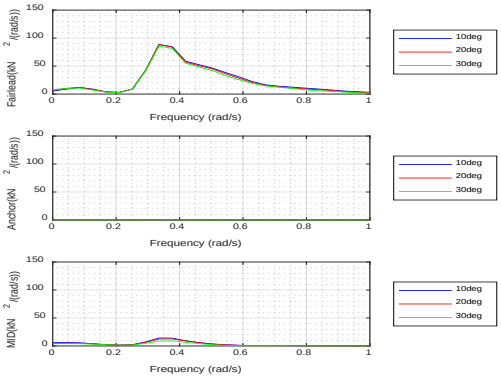

(b) Post-failure fairlead, anchor, MID on power cable

Figure 15: Frequency-domain effective tension of the power cable under the failure of Mooring Line #2

having a comparatively minor effect on the resonant characteristics of the vertical and pitch modes.

3.2.2 Mooring Line and Power Cable

Figure 14 presents the frequency spectrum analysis results of the effective tension in each mooring line (ML_#1–ML_#6) before and after the failure of ML_#2 (0–1800 and 1800–3600 s). Prior to the failure, distinct peaks were observed in most mooring lines at approximately 0.35–0.40 rad/s, which are attributed to the influence of the heave response of the floater. After the failure, all the mooring lines exhibited a substantial increase in energy in the low-frequency range below 0.1 rad/s, with apparent differences among the mooring line separation angles (10°, 20°, and 30°), particularly for ML_#1, ML_#3, ML_#5, and ML_#6. This indicates that the asymmetric restoring forces induced by the failure of ML_#2 became the dominant driver of the nonperiodic low-frequency motions.

Figure 15 illustrates the spatial redistribution of the spectral energy of the power cable after failure. In particular, at the cable locations on the side opposite to the failed line, a shift in the

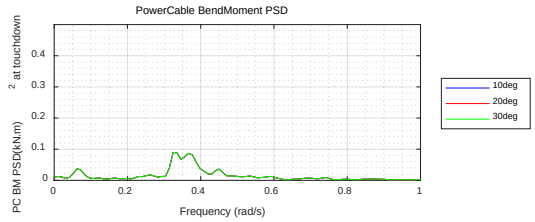

(a) Pre-failure touchdown point of the power cable

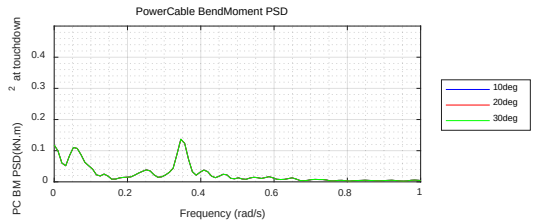

(b) Post-failure touchdown point of the power cable

Figure 16: Frequency-domain bending moment of the power cable under the failure of Mooring Line #2, TDP

rotation center and load redistribution reduced the transmitted motion, resulting in a decrease in the PSD across several frequency components.

Figure 16 shows the PSD of the bending moment at the TDP of the power cable. The energy concentration in the low-frequency range below 0.1 rad/s was observed both before and after the failure, with an increase in magnitude in the post-failure period. In addition, the small peak near 0.35–0.40 rad/s was attributed to the influence of wave loads.

4. Conclusion

This study analyzed the effect of the mooring line separation angle on the dynamic behavior of an FOWT and its power cable response under mooring line failure conditions.

The time-domain analysis showed:

- When all the mooring lines were intact, the separation angle had a minimal influence on the motion of the floater.
- However, after the failure of the mooring line ML_#2, the dynamic response became highly sensitive to the mooring layout. In particular, the 30° layout resulted in the largest increases in surge, sway, roll, and yaw owing to the greater asymmetry in the restoring forces.

The frequency-domain analysis showed:

- The heave and pitch exhibited apparent resonance peaks at approximately 0.3–0.4 rad/s.
- The surge, sway, roll, and yaw responses shifted to low-frequency ranges (<0.05 rad/s) after mooring failure, indicating slow, irregular motion.

The mooring and power cable analysis revealed:

- Increased tension was observed in other mooring lines owing to load redistribution owing to one-line failure, except for ML_#5 and ML_#6.
- A weak resonance peak (~0.35 rad/s) was transmitted throughout the power cable from the fairlead to the anchor with respect to the cable tension.
- The bending moment at the TDP of the power cable was largest under the 30° condition in the time domain.
- In the frequency domain, the 10° case showed the highest low-frequency spectral content, suggesting the long-term accumulation of repetitive bending.

The results emphasize the importance of the mooring configuration and the need for both time- and frequency-domain analyses. These findings provide critical insights into FOWT emergency response strategies and power cable fatigue life evaluations.

5. Future Work

Future studies will examine a range of mooring line failure scenarios and quantify the coupling effects among floating platforms within farm-scale configurations. Furthermore, the incorporation of active tension control strategies and a comprehensive evaluation of the long-term fatigue performance of power cables in irregular sea states will be performed.

Acknowledgement

This work was supported by the Korea Institute of Energy Technology Evaluation and Planning (KETEP) grant funded by the Korea government (MOTIE) (20213000000020, Development of core equipment and evaluation technology for construction of subsea power grid for offshore wind farm).

Author Contributions

Conceptualization, S. H. Park and W.C. Chung; Methodology, S. H. Park and W.C. Chung; Software, S. H. Park and W.C. Chung; Formal Analysis, S. H. Park; Investigation, S. H. Park and W.C. Chung; Resources, Y. H. Jung and W.C. Chung; Data Curation S. H. Park and W.C. Chung; Writing-Original Draft

Preparation, S. H. Park; Writing-Review & Editing, Y. H. Jung and W.C. Chung; Visualization, S. H. Park; Supervision, Y. H. Jung and W.C. Chung; Project Administration, Y. H. Jung and W.C. Chung; Funding Acquisition, Y. H. Jung and W.C. Chung.

References

[1] B. K. Jo, “Trends in promoting new energy industries for achieving carbon neutrality,” Electric World, vol. 70, no. 6, pp. 28-33, 2021 (in Korean).

[2] J. M. Kim and K. Y. Kim, “Economic analysis of renewable energy generation: Solar, wind, small hydropower, and biogas,” Journal of the Korean Solar Energy Society, vol. 28, no. 6, pp. 70-77, 2008 (in Korean).

[3] International Renewable Energy Agency (IRENA), World energy transitions outlook 2024: 1.5°C pathway, https://www.keei.re.kr/pdfOpen.es?bid=0014&list_#no=124476&seq=1, Accessed August 27, 2025.

[4] J. -S. Park, S. -H. Kim, and J. K. Seo, “Initial structural design approach for jacket-type substructure in 12 MW class offshore wind turbines considering soil stiffness,” Journal of Advanced Marine Engineering and Technology, vol. 47, no. 5, pp. 252-260, 2023.

[5] C. Min, D. Heo, and J. Park, “Economic analysis of offshore wind farms in Korea,” The Journal of the Korean Institute of Electrical Engineers, vol. 63, no. 9, pp. 1192-1198, 2014 (in Korean).

[6] Korea Research Institute of Ships & Ocean Engineering (KRISO), Development of a 15MW floating offshore wind platform in Korea, https://www.kriso.re.kr/gallery.es?act=view&b_#list=9&bid=0019&list_#no=694, Accessed August 27, 2025.

[7] S. Lee, S. Kim, and B. Kim, “Effect of wind-wave misalignment and yaw error on power performance and dynamic response of 15 MW floating offshore wind turbine,” New & Renewable Energy, vol. 20, no. 2, pp. 26-34, 2024.

[8] H. Ahn, Y. Ha, S. Park, and K. Kim, “A comparative study on the response characteristics of the semi-submersible platform of a 15 MW floating offshore wind turbine system in operational conditions,” Journal of Wind Energy, vol. 13, no. 4, pp. 17-25, 2022. (in Korean)

[9] J. Chen, C. Jin, and M. H. Kim, “Systematic comparisons among OpenFAST, Charm3D-FAST simulations and DeepCWind model test for 5 MW OC4 semisubmersible offshore wind turbine,” Ocean Systems Engineering, vol. 13, no. 2, pp. 173-193, 2023.

[10] C. Jin, I. Lee, J. Park, and M. Kim, “Dynamic behavior assessment of OC4 semi-submersible FOWT platform through Morison equation,” Journal of Ocean Engineering and Technology, vol. 37, no. 6, pp. 238-246, 2023.

[11] Y. H. Bae and H. Lee, “Transient effects of wind-wave hybrid platform in mooring line broken condition,” Journal of the Korean Society for Marine Environment & Energy, vol. 19, no. 2, pp. 129-136, 2016.

[12] Orcina, “OrcaFlex example: [K03 15MW semi-sub FOWT] (Version 1.1.3)”, https://www.orcina.com/, Accessed August 27, 2025.

[13] M. Rentschler, F. Adam, P. Chainho, K. Krugel, and P. C. Vicente, “Parametric Study of Dynamic Inter-Array Cable Systems for Floating Wind Applications,” Proceedings of OMAE 2020.

[14] M. G. Lee, K. H. Jung, S. B. Park, B. S. Yoo, and Y. S. Chung, “Extreme mooring analysis of a turret-moored LNG-FSRU,” Journal of the Society of Naval Architects of Korea, vol. 53, no. 5, pp. 435–446, 2016 (in Korean).